Supporting Information

Exploring the role of sandwich-type polyoxometalates in $\{K_{10}(PW_9O_{34})_2M_4(H_2O)_2\}$@PCN–222 (M=Mn, Ni, Zn) for electroreduction of CO_2 to CO

Meng-Ting Peng, Chuang Chen, Yan Zhang, Jia-Yu Xu, Yun-Lei Teng*, Bao-Xia Dong*

School of Chemistry and Chemical Engineering, Yangzhou University, Yangzhou, 225002, Jiangsu, PR China.

*Corresponding authors.

E-mail addresses: bxdong@yzu.edu.cn (B-X. Dong), ylteng@yzu.edu.cn (Y.-L. Teng)

Contents:

1. Figure S1. IR spectra of the composites in comparison to the precursor and each sandwich-type POM, (a) $P_2W_{18}Mn_4$@PCN–222; (b) $P_2W_{18}Ni_4$@PCN–222; (c) $P_2W_{18}Zn_4$@PCN–222.

2. Figure S2. UV spectra of the composites in comparison to the precursor and each sandwich-type POM, (a) $P_2W_{18}Mn_4$@PCN–222; (b) $P_2W_{18}Ni_4$@PCN–222; (c) $P_2W_{18}Zn_4$@PCN–222, in CH_2Cl_2.

3. Figure S3. The UV spectra and standard curves of $P_2W_{18}Mn_4$@PCN–222 (a,b), $P_2W_{18}Ni_4$@PCN–222 (c,d) and $P_2W_{18}Zn_4$@PCN–222 (e,f), in aqueous solution.

4. Table S1. ICP test for $P_2W_{18}M_4$@PCN–222 and $P_2W_{18}M_4$ precursor

5. **Table S2**. The specific surface area of PCN–222 and $P_2W_{18}M_4$@PCN–222

6. Figure S4. Nitrogen adsorption and desorption curves and pore size distribution of $P_2W_{18}Mn_4$@PCN–222 (a–b), $P_2W_{18}Ni_4$@PCN–222 (c–d), and $P_2W_{18}Zn_4$@PCN–222 (e–f).

7. Figure S5. SEM and elemental mapping images of (a) $P_2W_{18}Mn_4$@PCN–222, (b) $P_2W_{18}Ni_4$@PCN–222, and (c) $P_2W_{18}Zn_4$@PCN–222.

8. Figure S6. TGA curves and TG-Mass for PCN–222 and $P_2W_{18}M_4$@PCN–222 composites.

9. Table S3. C,H,N tests for $P_2W_{18}M_4$@PCN–222

10. Figure S7. (a) CV curves of $P_2W_{18}Ni_4$@PCN–222 compares to the MOF and POM precursors; CV (b) and LSV (c) curves of $P_2W_{18}Ni_4$@PCN–222 in CO_2-/N_2 saturated electrolyte; (d) LSV analysis of $P_2W_{18}Ni_4$@PCN–222 compares to the MOF and POM precursors.

11. Figure S8. (a) CV curves of $P_2W_{18}Zn_4$@PCN–222 compares to the MOF and POM precursors; CV (b) and LSV (c) curves of $P_2W_{18}Zn_4$@PCN–222 in CO_2-/N_2 saturated electrolyte; (d) LSV analysis of $P_2W_{18}Zn_4$@PCN–222 compares to the MOF and POM precursors.

12. Figure S9. Chronocurrent curves of (a) PCN–222; (b) $P_2W_{18}Mn_4$@PCN–222; (c) $P_2W_{18}Ni_4$@PCN–222; (d) $P_2W_{18}Zn_4$@PCN–222 at different potentials.

13. Figure S10. Comparative analysis of FE_{H2} in (a) $P_2W_{18}Mn_4$@PCN–222, (b) $P_2W_{18}Ni_4$@PCN–222, (c) $P_2W_{18}Zn_4$@PCN–222 vs. PCN–222 at different potentials.

14. Table S4. Product distribution of $P_2W_{18}M_4$@PCN–222/C (M=Mn, Ni, Zn) at an optimal potential of –0.60 V vs. RHE

15. Figure S11. Chronocurrent curves and product analysis of $P_2W_{18}M_4$ (M=Mn, Ni, Zn) from –0.55 to –0.65 V vs. RHE.

16. Figure S12. CV curves of (a) PCN–222; (b) $P_2W_{18}Mn_4$@PCN–222; (c) $P_2W_{18}Ni_4$@PCN–222; (d) $P_2W_{18}Zn_4$@PCN–222 with scan rate of 5~40 mV s^{-1}.

17. Figure S13. Current density of PCN–222 and $P_2W_{18}M_4$@PCN–222 at different scan rates.

18. Table S5. Electrochemically active surface area of the catalysts

19. Figure S14. Electrochemical impedance spectroscopy of PCN–222 and $P_2W_{18}M_4$@PCN–222.

20. Table S6. Resistances of PCN–222 and $P_2W_{18}M_4$@PCN–222 in the fitted circuit

21. Figure S15. Tafel slopes of PCN–222 and $P_2W_{18}M_4$@PCN–222.

22. Figure S16. Illustrations of each $P_2W_{18}M_4$-H_2–TCPP and the corresponding ECR intermediates (*COOH and *CO) configurations.

23. Figure S17. Free energies of hydrogen evolution process in $P_2W_{18}M_4$–H_2–TCPP and free ligand.

24. Table S7. Frontier molecular orbitals of $P_2W_{18}M_4$–H_2–TCPP and free ligand

25. Table S8. Frontier molecular orbital energies of $P_2W_{18}M_4$–H_2–TCPP and free ligand

26. Table S9. Comparison of FE_{CO} with other POM-based composites

27. Figure S18. The i-t curve of $P_2W_{18}Mn_4$@PCN–222 for 36 h and the product efficiency at –1.235 V vs. Ag/AgCl.

28. Figure S19. The photo images of $P_2W_{18}Mn_4$ (a,b) and $P_2W_{18}Mn_4$@PCN–222(c,d) loaded carbon

cloth electrode before and after the ECR test of 2 h.

29. Figure S20. SEM images of $P_2W_{18}Mn_4$@PCN–222 loaded carbon cloth electrode before and after the ECR test of 2 h (a,b) and 36 h (c,d).

30. Figure S21. XPS spectra of $P_2W_{18}Mn_4$@PCN–222 composite before and after electrolysis.

31. Figure S22. XPS spectra of $P_2W_{18}Mn_4$@PCN–222 composite before and after electrolysis: (a) P 2p; (b) W 4f; (c) Mn 2p; (d) Zr 3d.

32. Table S10. ICP results for each composite before and after electrolysis

33. Figure S23. Five kinds of possible interactions between $P_2W_{18}M_4$ and H_2–TCPP.

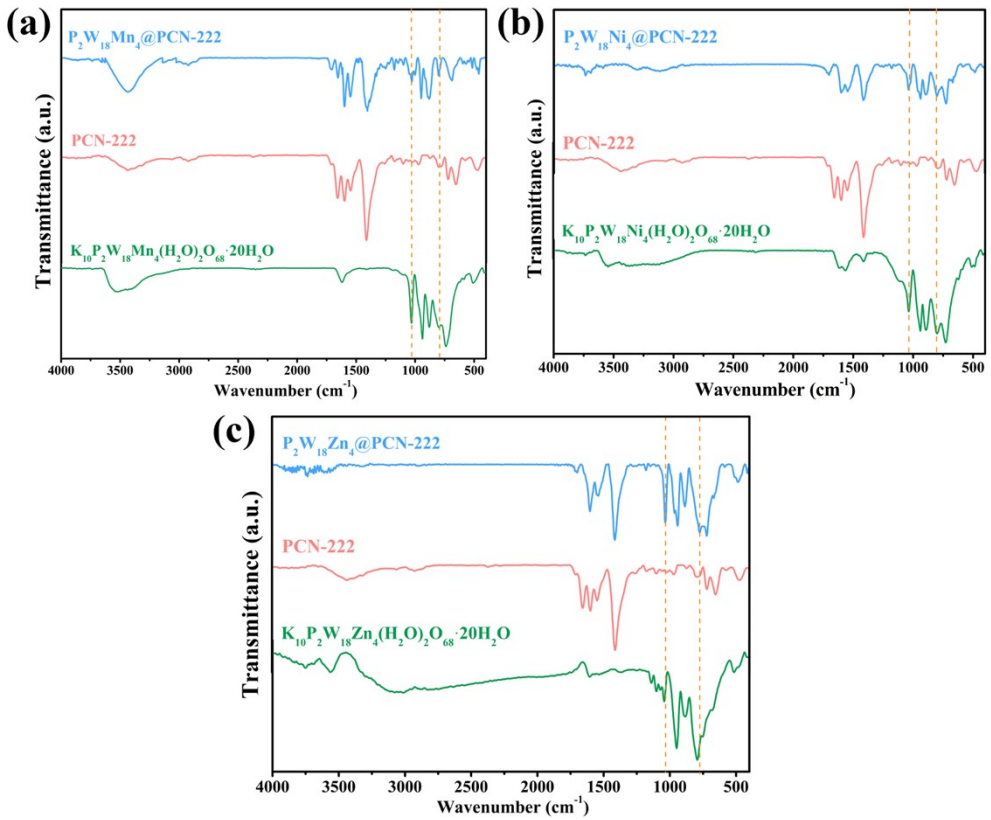

Figure S1. IR spectra of the composites in comparison to the precursor and each sandwich-type POM, (a) $P_2W_{18}Mn_4$@PCN–222; (b) $P_2W_{18}Ni_4$@PCN–222; (c) $P_2W_{18}Zn_4$@PCN–222.

As for $P_2W_{18}Mn_4$@PCN–222 (Figure S1a), 1029 cm^{-1} (P–O), 948 cm^{-1} (W–O), 877 and 798 cm^{-1} (W–O–W) belong to the characteristic peaks of $P_2W_{18}Mn_4$, 1402 cm^{-1} (C–C) and 1598 cm^{-1} (phenyl) belong to the characteristic peaks of PCN–222;

As for $P_2W_{18}Ni_4$@PCN–222 (Figure S1b), 1037 cm^{-1} (P–O), 939 cm^{-1} (W–O), 893 and 725 cm^{-1} (W–O–W) belong to the characteristic peaks of $P_2W_{18}Ni_4$, 1416 cm^{-1} (C–C) and 1587 cm^{-1} (phenyl) belong to the characteristic peaks of PCN–222;

As for $P_2W_{18}Zn_4$@PCN–222 (Figure S1c), 1033 cm^{-1} (P–O), 941 cm^{-1} (W–O), 887 and 775 cm^{-1} (W–O–W) belong to the characteristic peaks of $P_2W_{18}Zn_4$, 1416 cm^{-1} (C–C) and 1603 cm^{-1} (phenyl) belong to the characteristic peaks of PCN–222.[1–2]

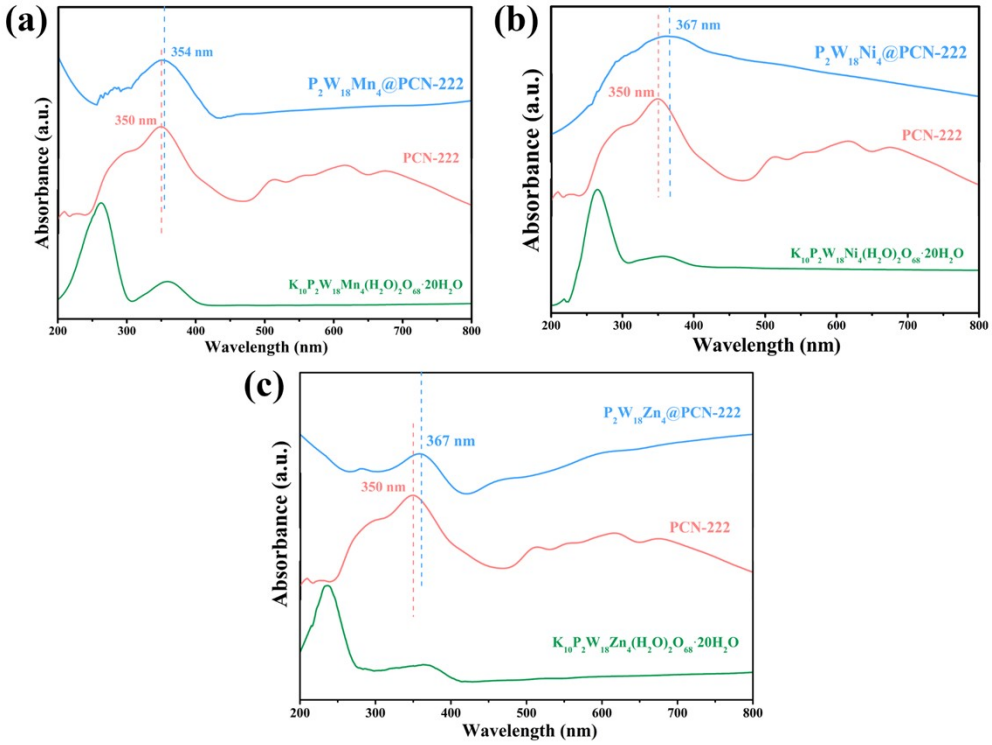

Figure S2. UV spectra of the composites in comparison to the precursor and each sandwich-type POM, (a) $P_2W_{18}Mn_4$@PCN–222; (b) $P_2W_{18}Ni_4$@PCN–222; (c) $P_2W_{18}Zn_4$@PCN–222, in CH_2Cl_2.

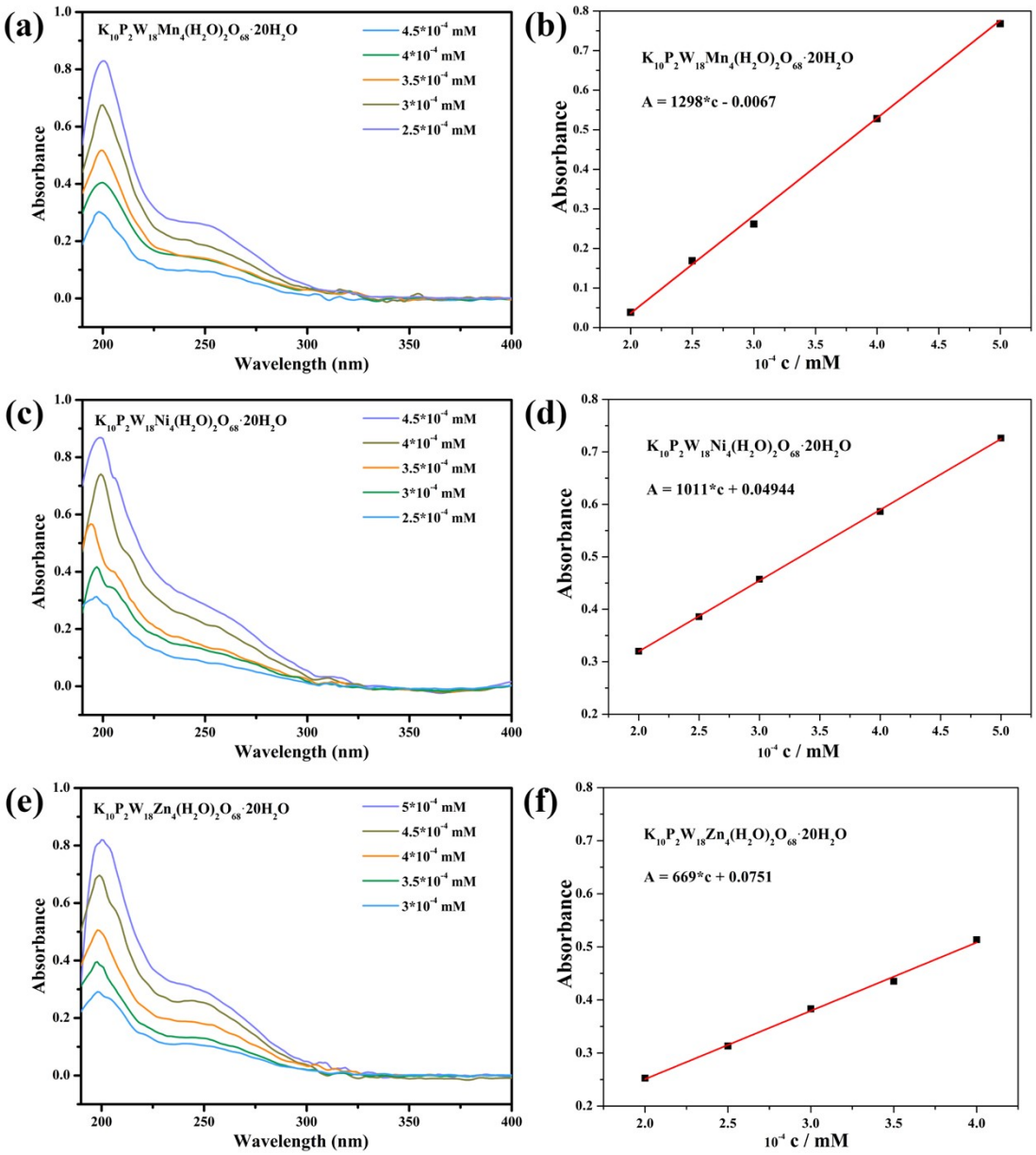

Figure S3. The UV spectra and standard curves of $P_2W_{18}Mn_4$@PCN–222 (a,b), $P_2W_{18}Ni_4$@PCN–222 (c,d) and $P_2W_{18}Zn_4$@PCN–222 (e,f), in aqueous solution.

Table S1. ICP test for $P_2W_{18}M_4$@PCN–222 and $P_2W_{18}M_4$ precursor

	P	W	Mn	Ni	Zn	Zr	P/W/M/Zr	$n_{P2W18M4}$/mg electrocatalyst /μmol	$P_2W_{18}M_4$ Loading/ unit cell
	mg/L								
$P_2W_{18}Mn_4$@ PCN–222	0.093	4.914	0.321			3.871	1: 8.9: 2.0: 14.1	0.0741	0.21
$P_2W_{18}Mn_4$	0.267	14.23	0.956				1: 9.0: 2.0		
$P_2W_{18}Ni_4$@ PCN–222	0.088	4.671		0.328		3.831	1: 9.1: 2.0: 15.0	0.0705	0.20
$P_2W_{18}Ni_4$	0.301	15.89		1.066			1: 8.9: 1.9		
$P_2W_{18}Zn_4$@ PCN–222	0.099	5.411			0.463	2.741	1: 9.2: 2.2: 9.4	0.0817	0.33
$P_2W_{18}Zn_4$	0.259	13.98			1.133		1: 9.1: 2.1		

Table S2. The specific surface area of PCN–222 and $P_2W_{18}M_4$@PCN–222

Catalysts	S_{BET} (m^2/g)
PCN–222	1998~2103
$P_2W_{18}Mn_4$@PCN–222	825
$P_2W_{18}Ni_4$@PCN–222	761
$P_2W_{18}Zn_4$@PCN–222	811

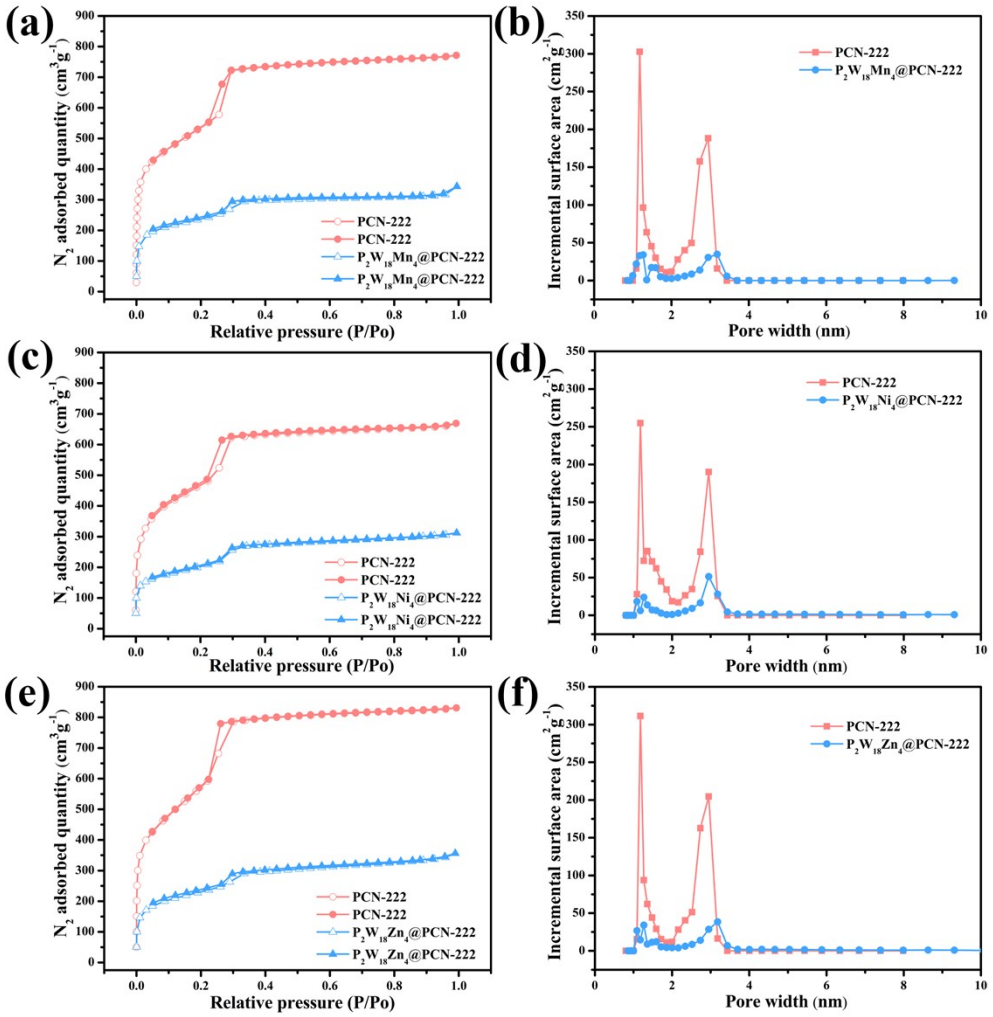

Figure S4. Nitrogen adsorption and desorption curves and pore size distribution of $P_2W_{18}Mn_4$@PCN–222 (a–b), $P_2W_{18}Ni_4$@PCN–222 (c–d), and $P_2W_{18}Zn_4$@PCN–222 (e–f).

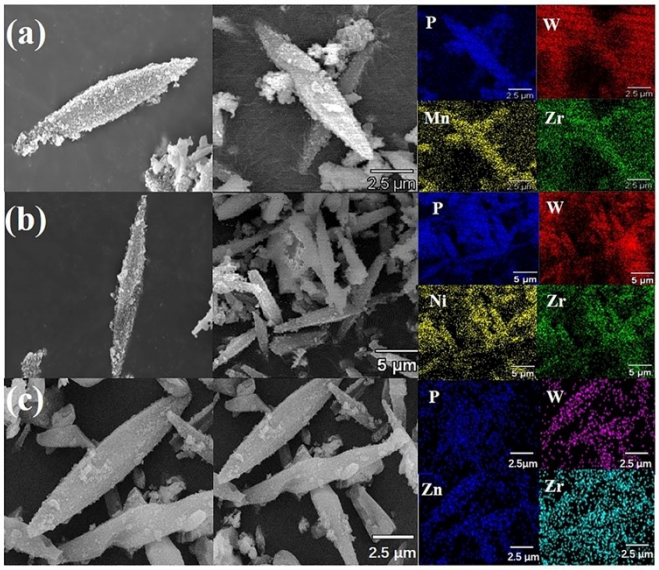

Figure S5. SEM and elemental mapping images of (a) $P_2W_{18}Mn_4$@PCN–222, (b)

$P_2W_{18}Ni_4$@PCN–222, and (c) $P_2W_{18}Zn_4$@PCN–222.

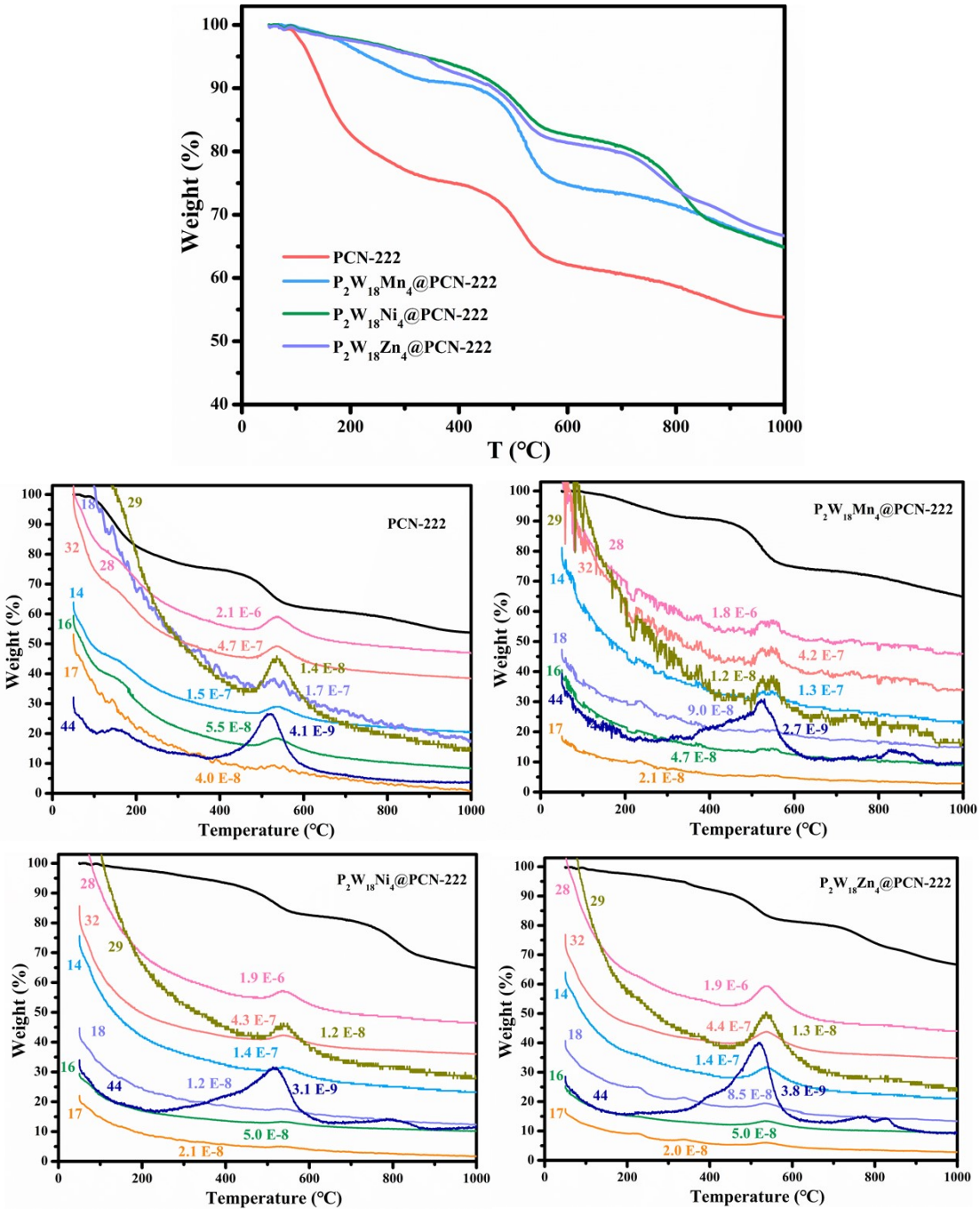

Figure S6. TGA curves and TG-Mass for PCN–222 and $P_2W_{18}M_4$@PCN–222 composites.

Table S3. C,H,N tests for $P_2W_{18}M_4$@PCN–222

	C wt%	H wt%	N wt%
$P_2W_{18}Mn_4$@PCN–222	33.46	2.14	3.30
$P_2W_{18}Ni_4$@PCN–222	33.94	2.06	3.31
$P_2W_{18}Zn_4$@PCN–222	28.21	2.34	2.73
PCN–222	46.68	2.96	4.52

We tentatively considered the following formulae:

$[Zr_6O_{16}H_{18}][C_{48}H_{26}N_4O_8]_2[KH_9P_2W_{18}Mn_4O_{68}(H_2O)_2]_{0.21}\cdot 2.8H_2O$

$[Zr_6O_{16}H_{18}][C_{48}H_{26}N_4O_8]_2[KH_9P_2W_{18}Ni_4O_{68}(H_2O)_2]_{0.20}\cdot 2.6H_2O$

$[Zr_6O_{16}H_{18}][C_{48}H_{26}N_4O_8]_2[KH_9P_2W_{18}Zn_4O_{68}(H_2O)_2]_{0.33}\cdot 5.9H_2O$

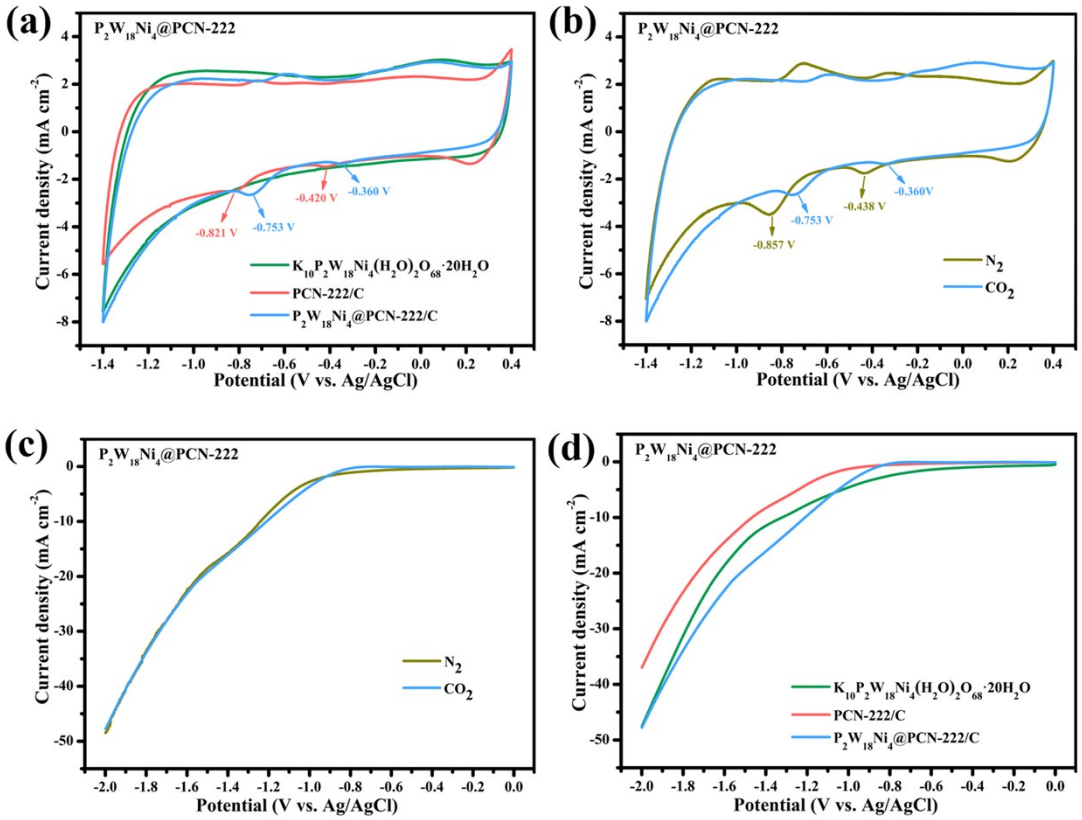

Figure S7. (a) CV curves of $P_2W_{18}Ni_4$@PCN–222 compares to the MOF and POM precursors in CO_2-saturated 0.5 M $KHCO_3$ solution; CV (b) and LSV (c) curves of $P_2W_{18}Ni_4$@PCN–222 in CO_2-/N_2 saturated electrolyte; (d) LSV analysis of $P_2W_{18}Ni_4$@PCN–222 compares to the MOF and POM precursors in CO_2-saturated electrolyte; sweep speed, 50 mV/s.

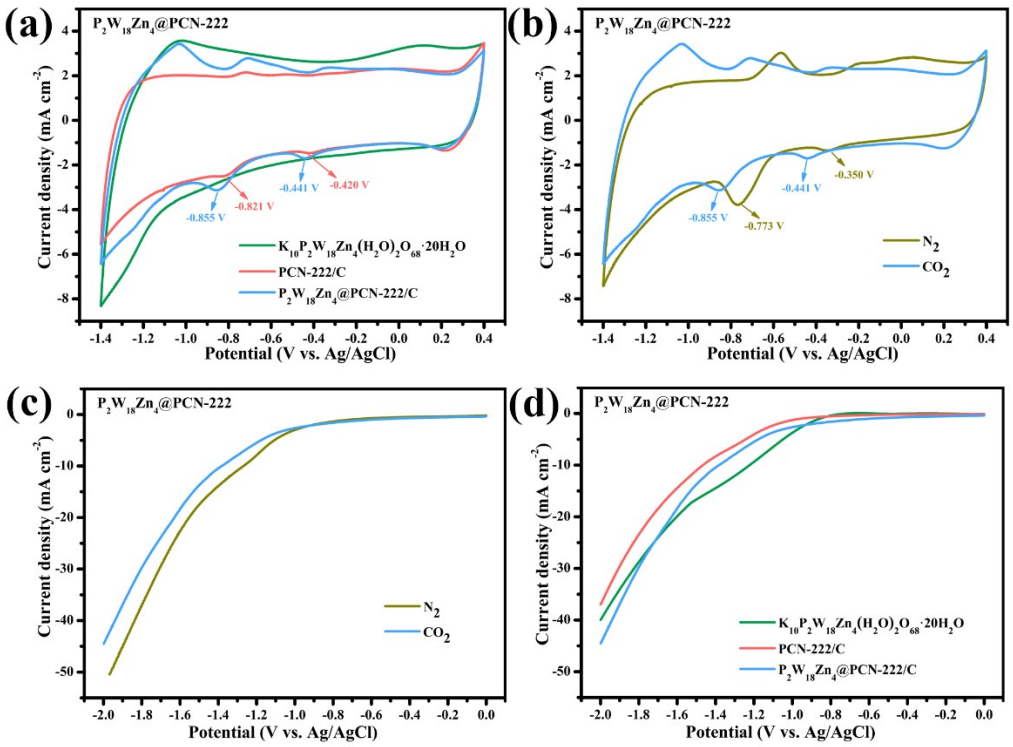

Figure S8. (a) CV curves of $P_2W_{18}Zn_4$@PCN–222 compares to the MOF and POM precursors in CO_2-saturated 0.5 M $KHCO_3$ solution; CV (b) and LSV (c) curves of $P_2W_{18}Zn_4$@PCN–222 in CO_2-/N_2 saturated electrolyte; (d) LSV analysis of $P_2W_{18}Zn_4$@PCN–222 compares to the MOF and POM precursors in CO_2-saturated electrolyte; sweep speed, 50 mV/s.

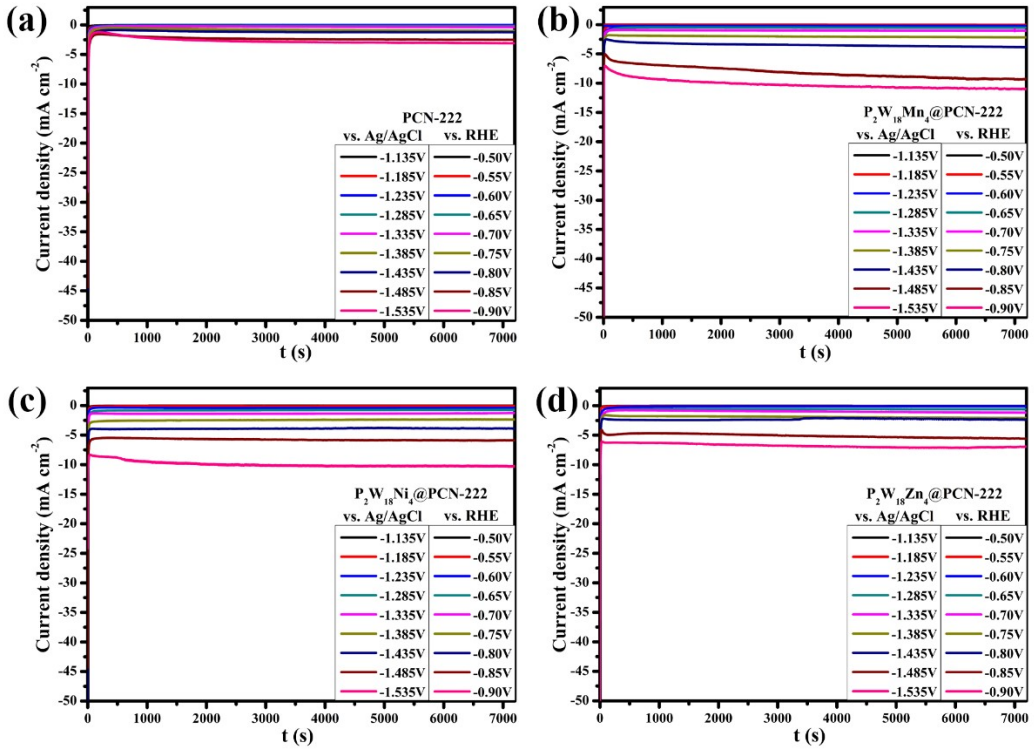

Figure S9. Chronocurrent curves of (a) PCN–222; (b) $P_2W_{18}Mn_4$@PCN–222; (c) $P_2W_{18}Ni_4$@PCN–222; (d) $P_2W_{18}Zn_4$@PCN–222 at different potentials.

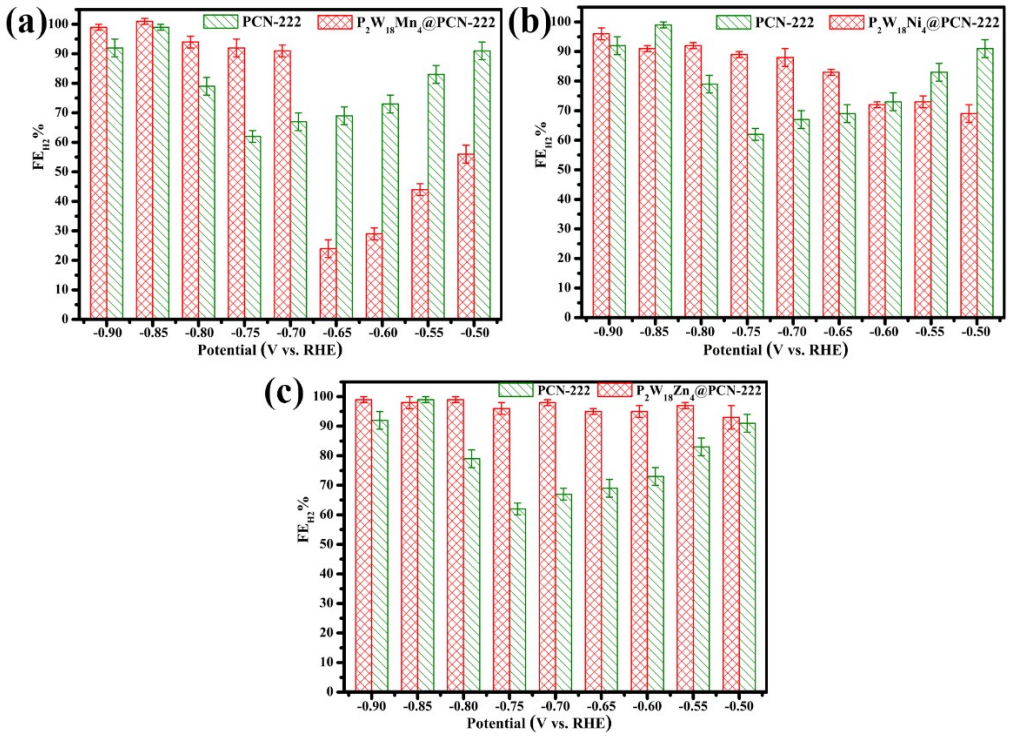

Figure S10. Comparative analysis of FE_{H2} in (a) $P_2W_{18}Mn_4$@PCN–222, (b) $P_2W_{18}Ni_4$@PCN–222, (c) $P_2W_{18}Zn_4$@PCN–222 vs. PCN–222 at different potentials.

Table S4. Product distribution of $P_2W_{18}M_4$@PCN–222 (M=Mn, Ni, Zn) at an optimal potential of –0.60 V vs. RHE

	PCN–222	$P_2W_{18}Mn_4$@ PCN–222	$P_2W_{18}Ni_4$@ PCN–222	$P_2W_{18}Zn_4$@ PCN–222
vs. Ag/AgCl (V)			–1.235	
vs. RHE (V)			–0.60	
FE_{H2} (%)	73.6	29.2	72.2	95.2
FE_{CO} (%)	18.1	72.6	26.9	3.5

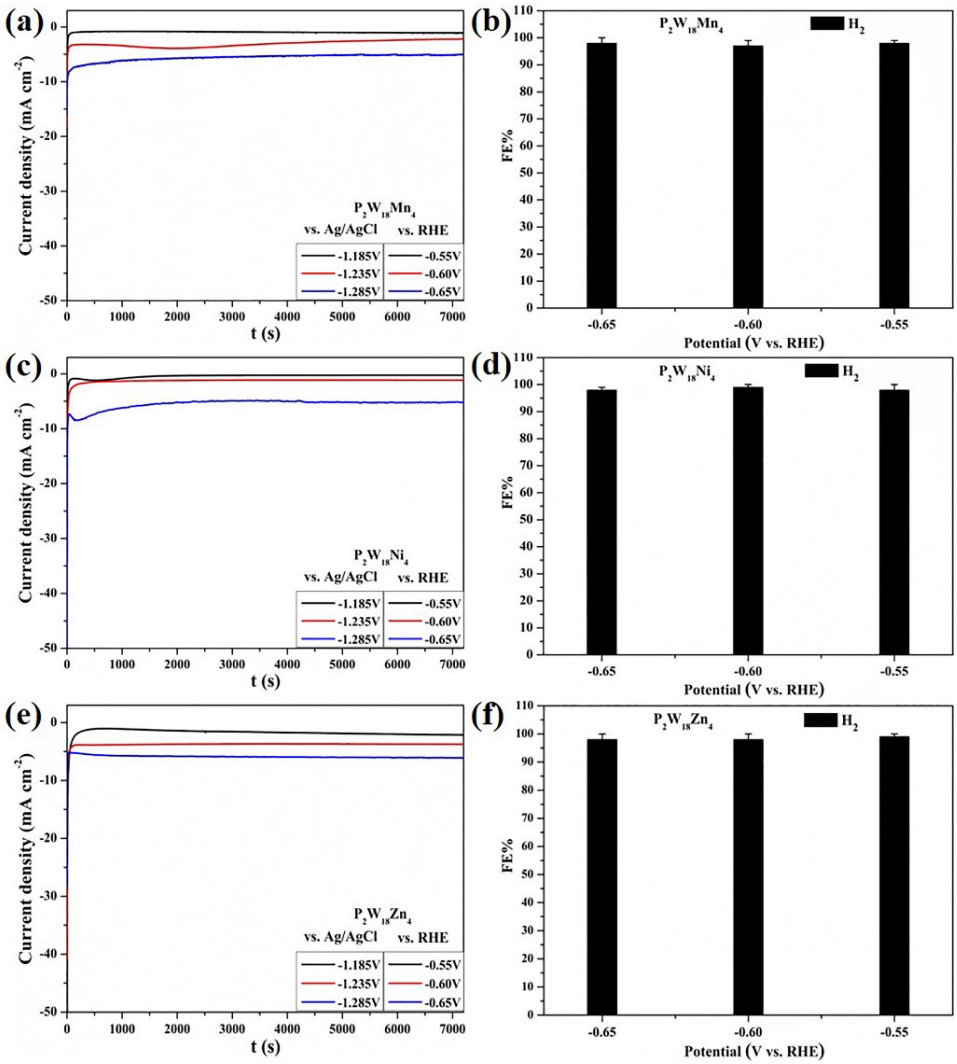

Figure S11. Chronocurrent curves and product analysis of $P_2W_{18}M_4$ (M=Mn, Ni, Zn) from –0.55 to –0.65 V vs. RHE.

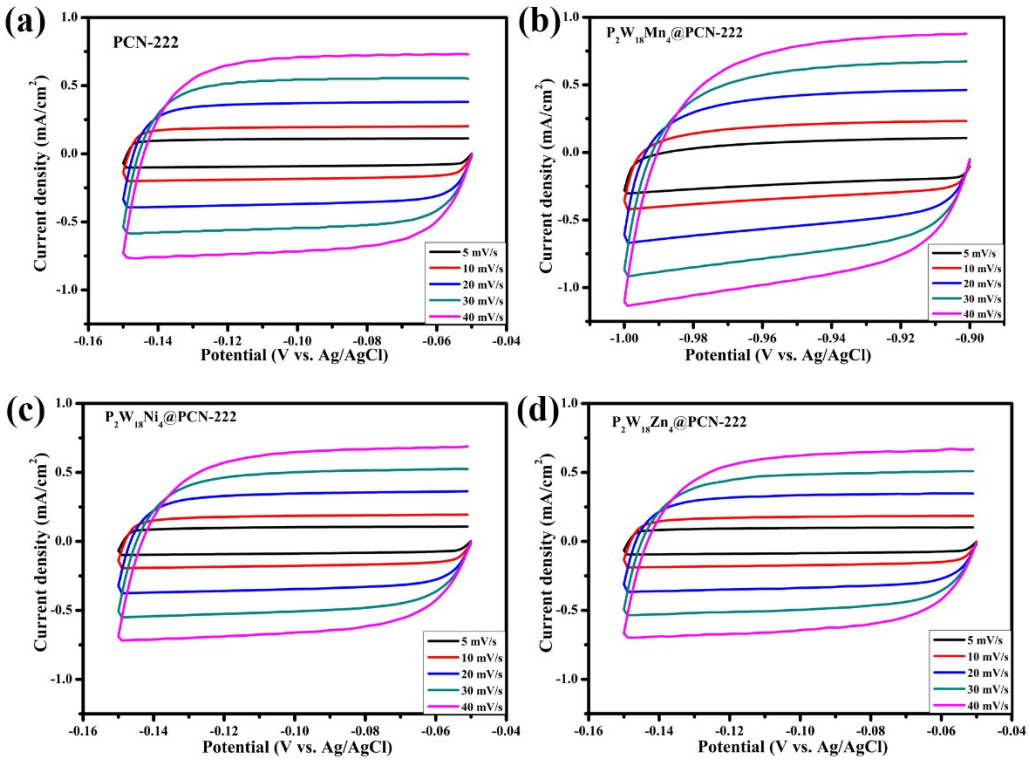

Figure S12. CV curves of (a) PCN–222; (b) $P_2W_{18}Mn_4$@PCN–222; (c) $P_2W_{18}Ni_4$@PCN–222; (d) $P_2W_{18}Zn_4$@PCN–222 with scan rate of 5~40 mV s^{-1}.

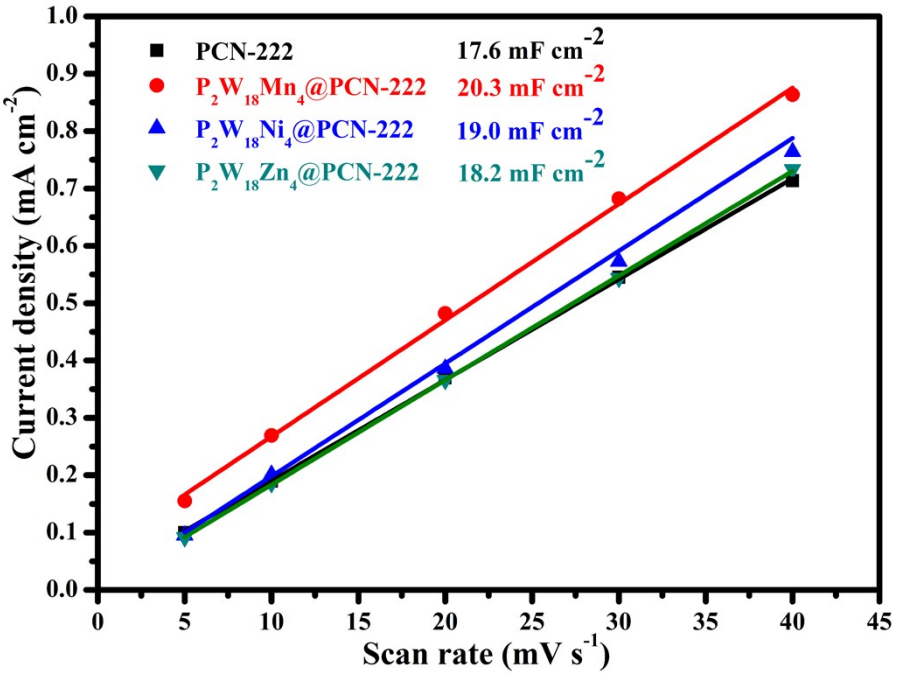

Figure S13. Current density of PCN–222 and $P_2W_{18}M_4$@PCN–222 at different scan rates.

Table S5. Electrochemically active surface area of the catalysts

Catalysts	C_{dl} (mF cm^{-2})	ECSA (cm^2)
PCN–222	17.6	878.0
$P_2W_{18}Mn_4$@PCN–222	20.3	1013.5
$P_2W_{18}Ni_4$@PCN–222	19.0	948.0
$P_2W_{18}Zn_4$@PCN–222	18.2	911.5

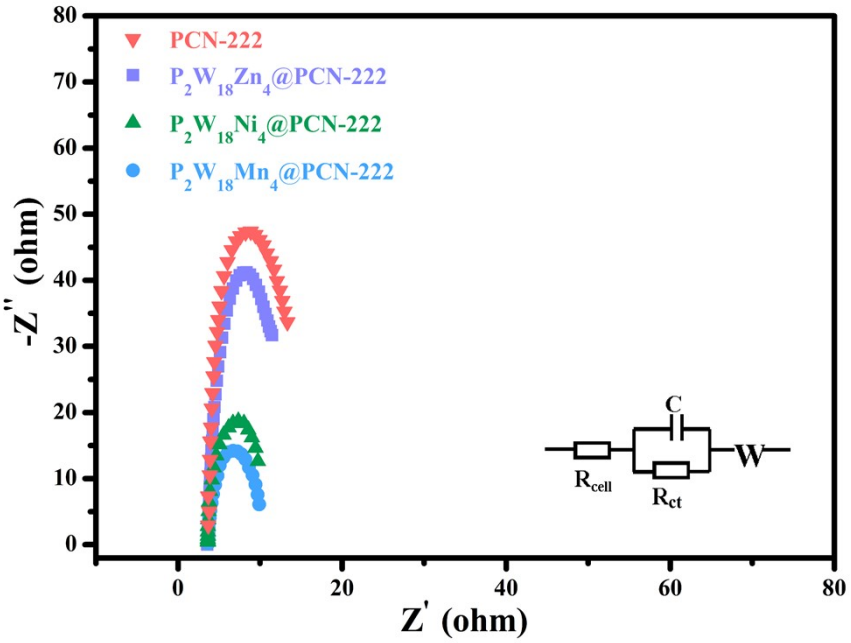

Figure S14. Electrochemical impedance spectroscopy of PCN–222 and $P_2W_{18}M_4$@PCN–222.

Table S6. Resistances of PCN–222 and $P_2W_{18}M_4$@PCN–222 in the fitted circuit

Catalysts	R_{cell} (Ω)	R_{ct} (Ω)
PCN–222	6.7	78.4
$P_2W_{18}Mn_4$@PCN–222	3.5	12.1
$P_2W_{18}Ni_4$@PCN–222	3.8	18.2
$P_2W_{18}Zn_4$@PCN–222	5.3	72.3

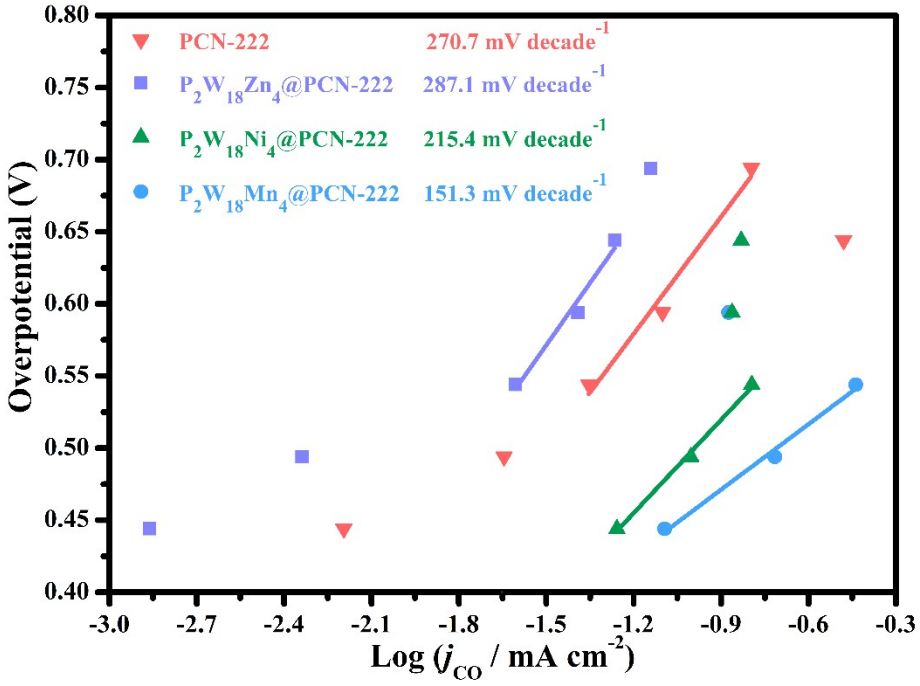

Figure S15. Tafel slopes of PCN–222 and $P_2W_{18}M_4$@PCN–222.

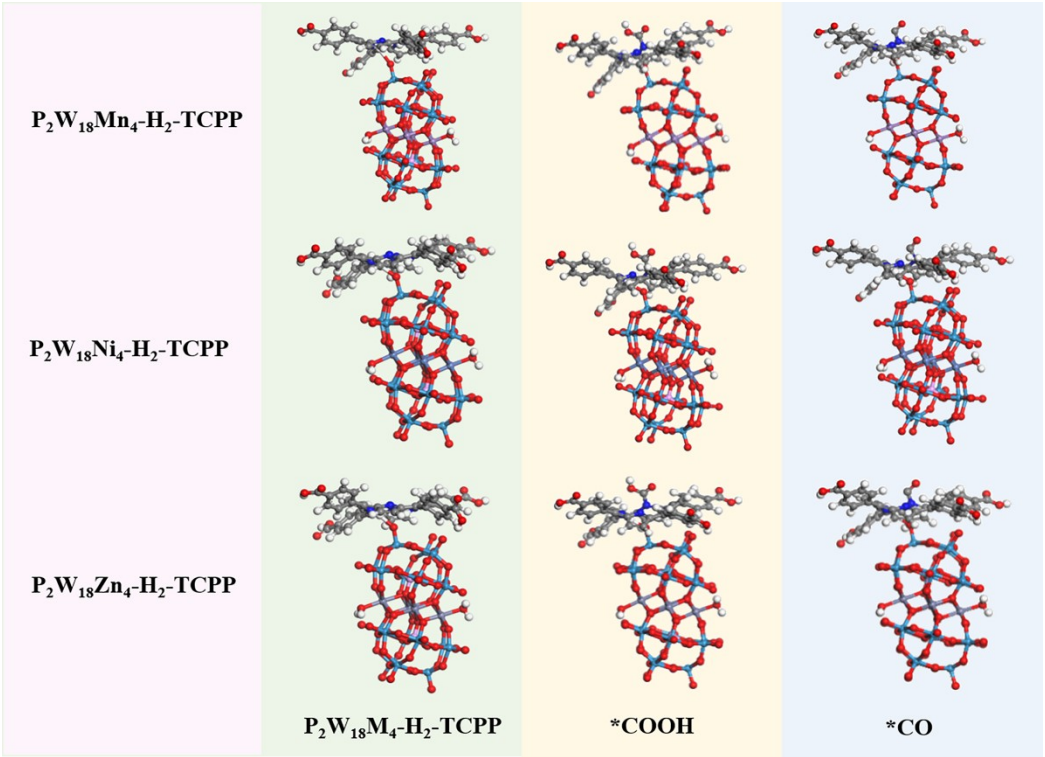

Figure S16. Illustrations of each $P_2W_{18}M_4$-H_2–TCPP and the corresponding ECR intermediates (*COOH and *CO) configurations.

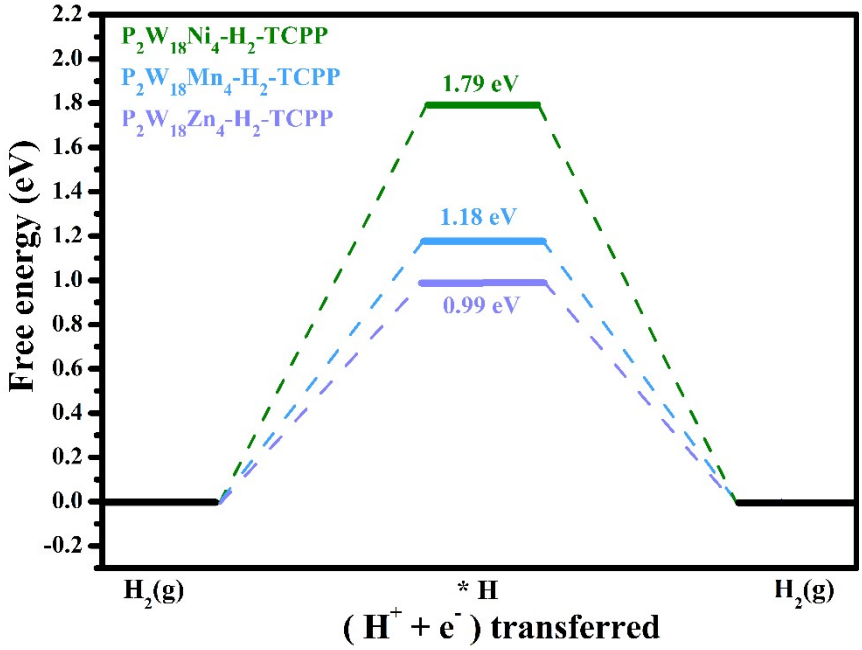

Figure S17. Free energies of hydrogen evolution process in $P_2W_{18}M_4$–H_2–TCPP and free ligand.

Table S7. Frontier molecular orbitals of $P_2W_{18}M_4$–H_2–TCPP and free ligand

	HOMO	LUMO
$P_2W_{18}Mn_4$–H_2–TCPP	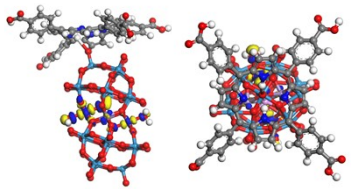	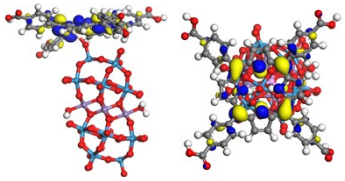
$P_2W_{18}Ni_4$–H_2–TCPP	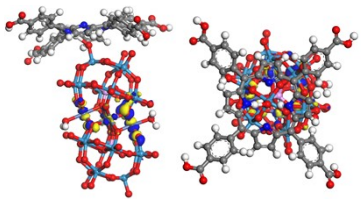	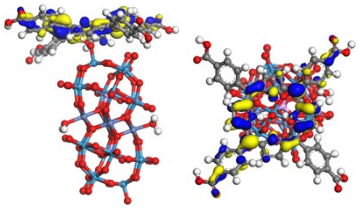
$P_2W_{18}Zn_4$–H_2–TCPP	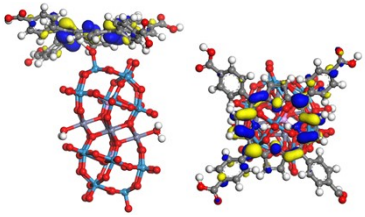	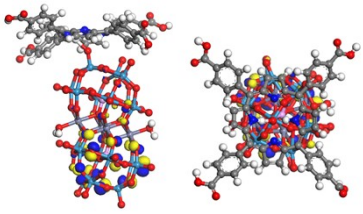
H_2–TCPP	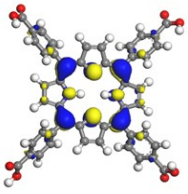	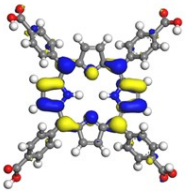

Table S8. Frontier molecular orbital energies of $P_2W_{18}M_4$–H_2–TCPP and free ligand

	E_{HOMO} (eV)	E_{LUMO} (eV)	ΔE_{L-H} (eV)	$E_{onse-red}$ (V vs Ag/AgCl)[a]	E_{LUMO} (eV)[b]
$P_2W_{18}Mn_4$–H_2–TCPP	–0.172	–0.148	0.024	–0.273	–4.447
$P_2W_{18}Ni_4$–H_2–TCPP	–0.163	–0.131	0.032	–0.284	–4.436
$P_2W_{18}Zn_4$–H_2–TCPP	–0.167	–0.119	0.046	–0.368	–4.352
H_2–TCPP	–0.191	–0.129	0.0623	–0.352	–4.368

[a] Onset reduction potential measured by cyclic voltammetry.

[b] E_{LUMO}= –($E_{onset(red)}$+4.72) eV

The DFT calculation gave the LUMO level trend of $P_2W_{18}Mn_4$–H_2–TCPP< $P_2W_{18}Ni_4$–H_2–TCPP <H_2–TCPP< $P_2W_{18}Zn_4$–H_2–TCPP. A lower LUMO level means that the composite is more electron-hungry, and therefore, it will be reduced more easily. Hence, we can conclude that their formal reduction potential would follow the trends of $P_2W_{18}Zn_4$–H_2–TCPP< H_2–TCPP< $P_2W_{18}Ni_4$–H_2–TCPP< $P_2W_{18}Mn_4$–H_2–TCPP (less negative). The CV measurement brings out consistent results of –0.441 V ($P_2W_{18}Zn_4$–H_2–TCPP), –0.420 V (H_2–TCPP), –0.360 V ($P_2W_{18}Ni_4$–H_2–TCPP), and –0.352 V ($P_2W_{18}Mn_4$–H_2–TCPP). Moreover, from the onset reduction potentials in the cyclic voltammogram, the LUMO levels can be estimated according to the following equations: E_{LUMO}= –($E_{onset(red)}$+4.72) eV.[3,4] It presents the same trends of $P_2W_{18}Mn_4$–H_2–TCPP< $P_2W_{18}Ni_4$–H_2–TCPP <H_2–TCPP< $P_2W_{18}Zn_4$–H_2–TCPP with those of the DFT results.

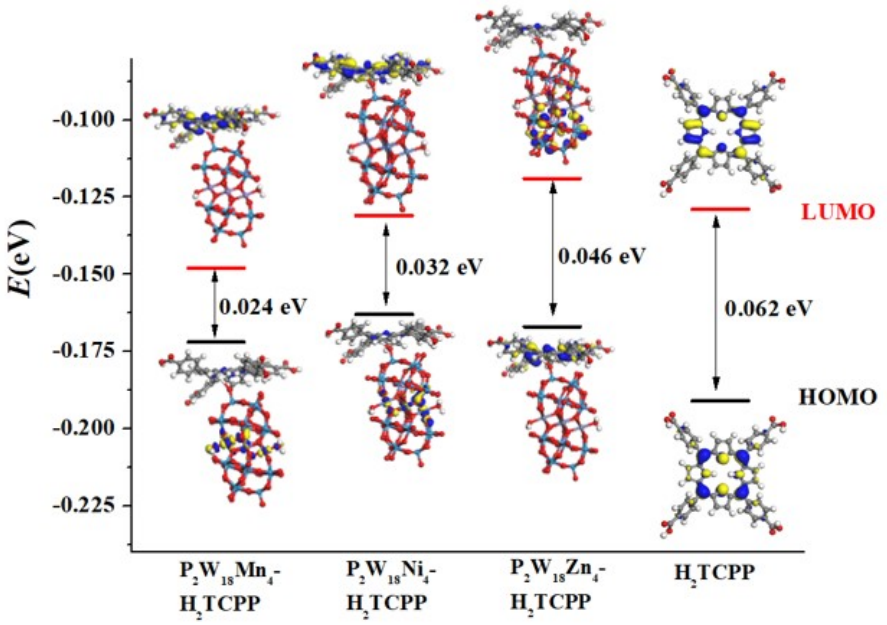

Table S9. Comparison of ECR performance with some electron-rich encapsulated composites

Catalysts	Electrolyte	Potential [η] (V)	Stability	Product	FE (%)	Ref.
$P_2W_{18}Mn_4$@PCN–222	0.5 M $KHCO_3$	–0.60 V vs. RHE [0.494]	36 h	CO	72	This work
$P_2W_{18}Ni_4$@PCN–222		–0.60 V vs. RHE [0.494]			26	
$P_2W_{18}Zn_4$@PCN–222		–0.70 V vs. RHE [0.594]			5	
$[Mn^{III}TRP]^{5+}/[SiW_{12}O_{40}]^{4-}$	0.1 M $NaClO_4$	−0.8 V vs Ag/AgCl		HCOOH		6
$[Ni^{II}TRP]^{4+}/[SiW_{12}O_{40}]^{4-}$				CO		
$[Zn^{II}TRP]^{4+}/[SiW_{12}O_{40}]^{4-}$				CH_3OH		
AgNC@BSA–SiW_{12}	0.1 M Bu_4NPF_6	−0.69 V vs RHE	5 h	CO	76	7
Ag–PMo_{12}	0.1 M Bu_4NPF_6	−1.90 V vs $Fc^{0/+}$	3 h	CO	90	8
Co–PMOF	0.5 M $KHCO_3$	–0.80 V vs RHE	36 h	CO	99	9
Fe–PMOF		–0.70 V vs RHE			29	
Ni–PMOF		–0.80 V vs RHE			19	
Zn–PMOF		–0.90 V vs RHE			1	
$[H_2PW_{11}O_{39}\{Rh^{III}Cp^*(OH_2)\}]^{3-}$	$TBABF_4$	–1.60 V vs NHE	5 h	$HCOO^-$	5	10
SiW_{12}–MnL	0.5 M $KHCO_3$	–0.72 V vs. RHE	12 h	CO	95	11
PW_{12}–MnL		–0.72 V vs. RHE			80	
PMo_{12}–MnL		–0.64 V vs. RHE			65	
Mo8@Cu/TNA	$NaHCO_3$	−1.13 V vs RHE		CH_3COO^-	49	12
Zn−CoTAPc/PMo_{12}	0.5 M $KHCO_3$	–0.70 V vs RHE	12 h	CO	96	13
H–POM@PCN–222–Co	0.5 M $KHCO_3$	–0.80 V vs RHE	10 h	CO	96	14
H–POM@PCN–222–Fe		–0.80 V vs RHE			42	
H–POM@PCN–222–Mn		–0.80 V vs RHE			31	
H–POM@PCN–222–Ni		–0.90 V vs RHE			41	

PCN–222/CNT		–0.65 V vs. RHE [0.544]			81	
PCN–222(Mn)/CNT		–0.60 V vs. RHE [0.494]			88	
PCN–222(Co)/CNT	0.5 M $KHCO_3$	–0.65 V vs. RHE [0.544]		CO	89	5
PCN–222(Ni)/CNT		–0.80 V vs. RHE [0.694]			52	
PCN–222(Zn)/CNT		–0.70 V vs. RHE [0.594]			92	
$CoCp_2$@MOF–545		–0.70 V vs RHE			20	
$CoCp_2$@MOF–545–Co	0.5 M $KHCO_3$	–0.90 V vs RHE	8 h	CO	97	15
$FeCp_2$@MOF–545–Co		–0.80 V vs RHE			94	
$NiCp_2$@MOF–545–Co		–0.80 V vs RHE			82	
TTF–Por(Co)–COF	0.5 M $KHCO_3$	–0.70 V vs RHE	10 h	CO	95	16
TCPP(Co)/Zr–BTB –PSABA	0.5 M $KHCO_3$	–0.77 V vs RHE	18 h	CO	85	17
ZrPP–1–Co@r–GO		–0.60 V vs. RHE	10 h		82	
ZrPP–1–Ni@r–GO	0.5 M $KHCO_3$	–0.60 V vs. RHE			78	18
ZrPP–1–Zn@r–GO		–0.60 V vs. RHE			16	
NiPor–CTF	0.5 M $KHCO_3$	–0.90 V vs. RHE	20 h	CO	97	19
PPy@MOF–545–Co	0.1 M $KHCO_3$	–0.80 V vs. RHE	10 h	CO	98	20

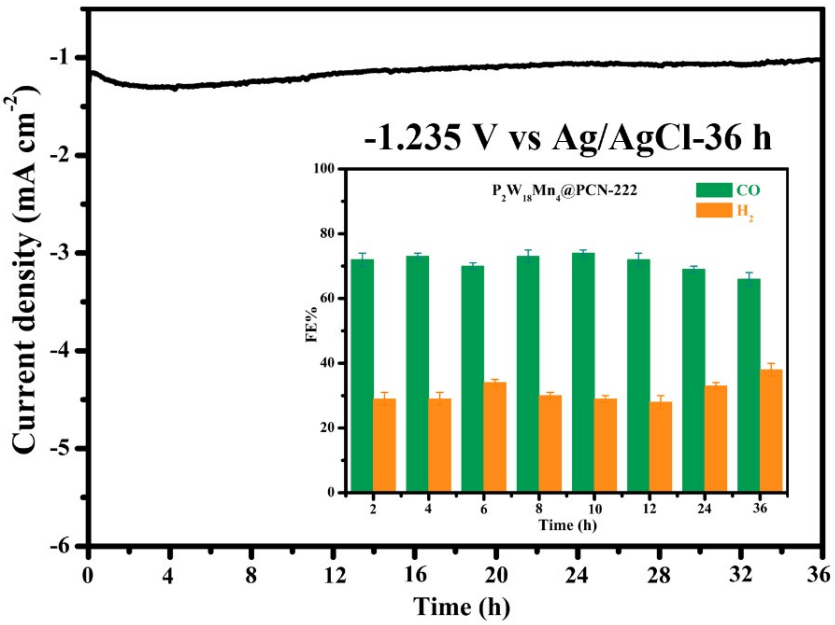

Figure S18. The i-t curve of $P_2W_{18}Mn_4$@PCN–222 for 36 h and the product efficiency at –1.235 V vs. Ag/AgCl.

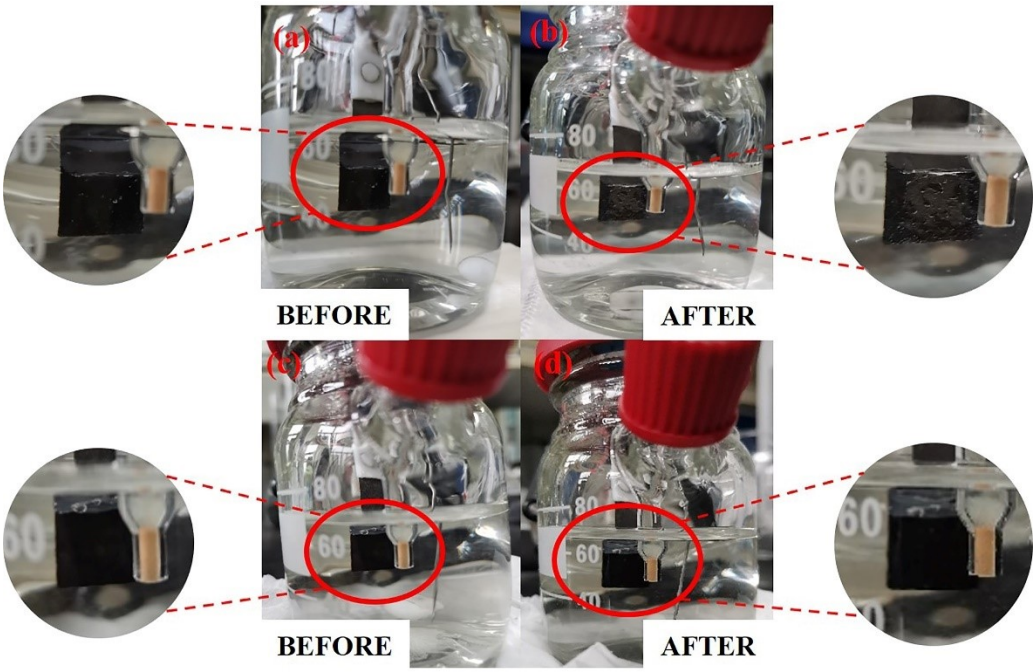

Figure S19. The photo images of $P_2W_{18}Mn_4$ (a,b) and $P_2W_{18}Mn_4$@PCN–222(c,d) loaded carbon cloth electrode before and after the ECR test of 2 h.

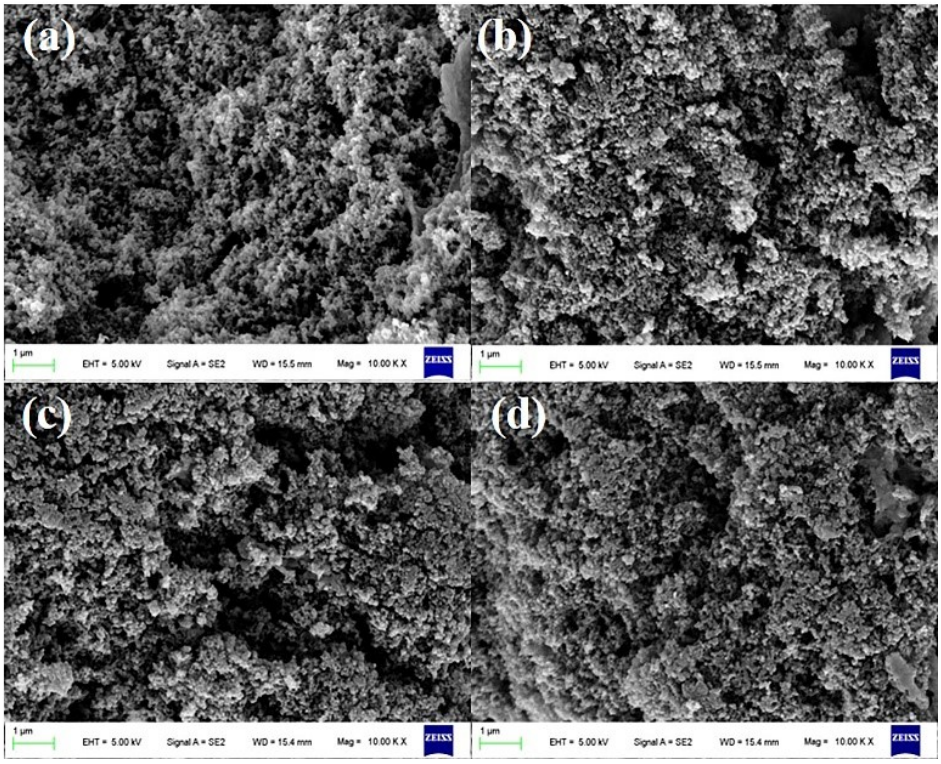

Figure S20. SEM images of $P_2W_{18}Mn_4$@PCN–222 loaded carbon cloth electrode before and after the ECR test of 2 h (a,b) and 36 h (c,d).

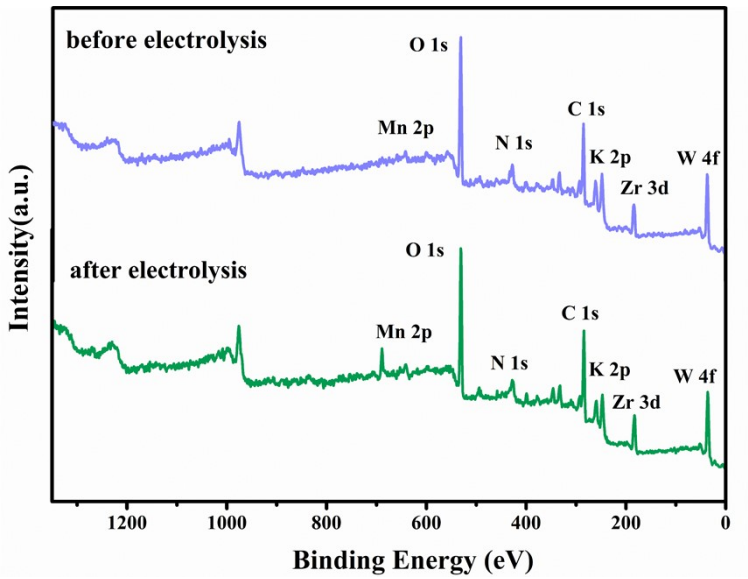

Figure S21. XPS spectra of $P_2W_{18}Mn_4$@PCN–222 composite before and after electrolysis.

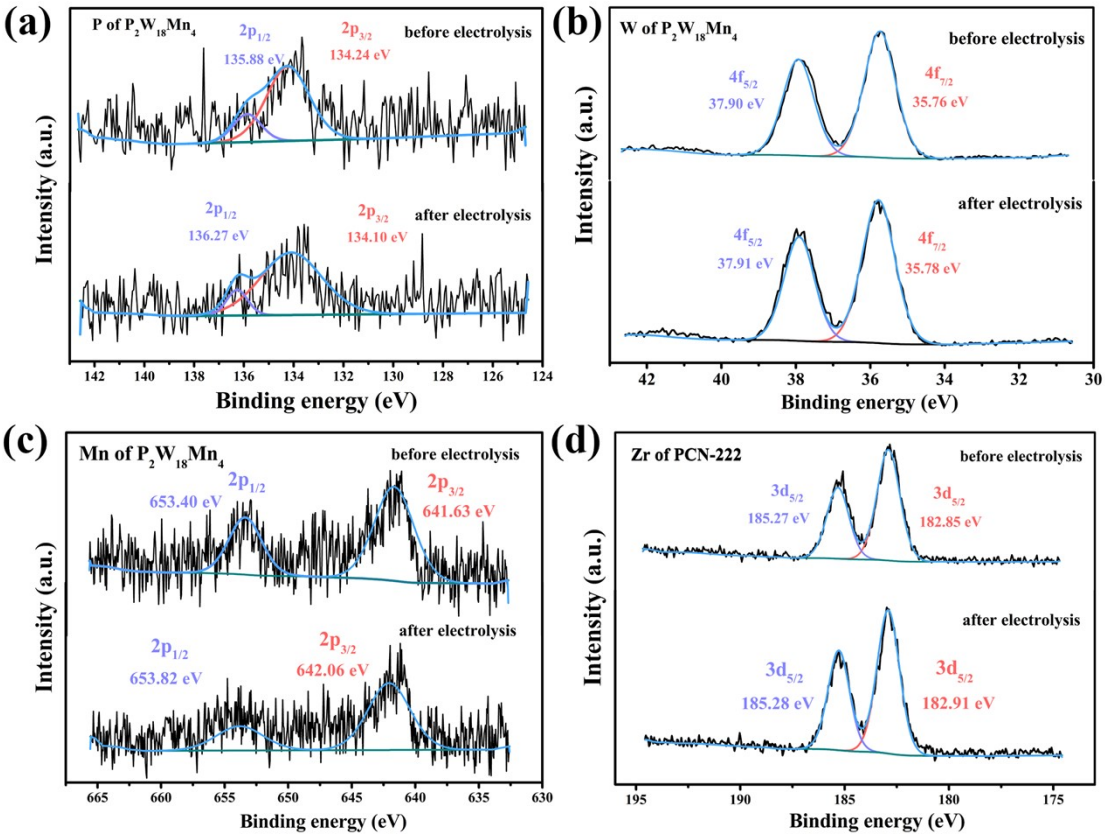

Figure S22. XPS spectra of $P_2W_{18}Mn_4$@PCN–222 composite before and after electrolysis: (a) P 2p; (b) W 4f; (c) Mn 2p; (d) Zr 3d.

About the stability test:

When directly using the potassium salts of $P_2W_{18}M_4$ as the electrocatalyst to mix with the Nafion ink, we can notice the exfoliation of the catalyst layer from the carbon cloth after 2 h electrolysis (Figure S19a,b), hinting at the instability of the $P_2W_{18}M_4$ under this experimental condition. In contrast, the incorporation of $P_2W_{18}M_4$ inside the framework of PCN–222 could provide super-stability, as shown in Figure S19c-d. After the electrocatalysis test, the solution has no color change. Since the electrode is made by mixing with the Nafion ink and loaded on the carbon cloth, all of the diffraction peaks of PCN–222 would be covered by the signal of C. Therefore, we could not obtain support from the XRD analysis. The same situation happens to the IR analysis. To support the stability of the electrode, we measured the ICP, XPS, and SEM before and after electrolysis. The SEM images for the $P_2W_{18}Mn_4$@PCN–222 modified electrode have minor changes even over 36 h electrolysis, supporting the excellent stability of the composite (Figure S20). For the XPS spectra,

the binding energies of P, W, Mn, Zr signals have little change before and after electrolysis (Figure S21-S22).

For the ICP test, we used the sample which has been deposited on the carbon cloth. We scraped off the composite before and after electrolysis and then tested the metal content. We can conclude that the Nafion membrane and the PCN-222 framework could well protect against the leaching of polyanions. The content of P, W, Mn, and Zr has little change before and after electrolysis.

Table S10. ICP results for each composite before and after electrolysis

	K	P	W	Mn/Ni/Zn	Zr
			mg/L		
$P_2W_{18}Mn_4$@PCN–222 **(before electrolysis)**	0.030	0.045	2.385	0.157	1.684
$P_2W_{18}Mn_4$@PCN–222 **(after electrolysis 36 h)**	0.026	0.047	2.390	0.159	1.679
$P_2W_{18}Ni_4$@PCN–222 **(before electrolysis)**	0.027	0.046	2.420	0.170	1.895
$P_2W_{18}Ni_4$@PCN–222 **(after electrolysis 2 h)**	0.021	0.043	2.399	0.170	1.876
$P_2W_{18}Zn_4$@PCN–222 **(before electrolysis)**	0.032	0.052	2.693	0.196	1.364
$P_2W_{18}Zn_4$@PCN–222 **(after electrolysis 2 h)**	0.033	0.050	2.690	0.198	1.365

About the screening of the computation models:

After several trials, we finally confirmed the current computational models, whereas the terminal oxygen tends to interact with the N–H in the porphyrin ring. The porphyrin molecules act as active centers in ECR, which has been proposed in many experiments and theoretical works.[5,14–15,21] Moreover, on the basis of the experimental study, the POMs alone have been confirmed inactive for ECR. The incorporated POM prefers to stay in the hexagonal channels of the PCN-222 and adjusts itself close to the porphyrin center.[14,15] In view of this, we adopted finite cluster calculations for saving computing tasks and proposed several possible interactions between H_2–TCPP and $P_2W_{18}M_4$ (Figure S23), (a) M–OH_2–N (strong interaction); (b) M–OH_2···N (weak interaction); (c) W=O···N–H (weak interaction, W=O comes from the polar $\{W_3O_{10}\}$ cluster); (d) W=O–N–H (strong interaction, W=O comes from the polar $\{W_3O_{10}\}$ cluster); (e) W=O–N–H (strong interaction, W=O comes from the equatorial $\{W_3O_{10}\}$ cluster). However, only the proposed interactions of d and e could be structurally optimized. Other configurations suffer from severe deformation. The optimized configurations of d and e were applied for further energy barrier calculation. The free energy diagrams indicate that the e configuration contradicts the experimental results. Therefore, the configuration of d is screened as a potential interaction for further investigation.

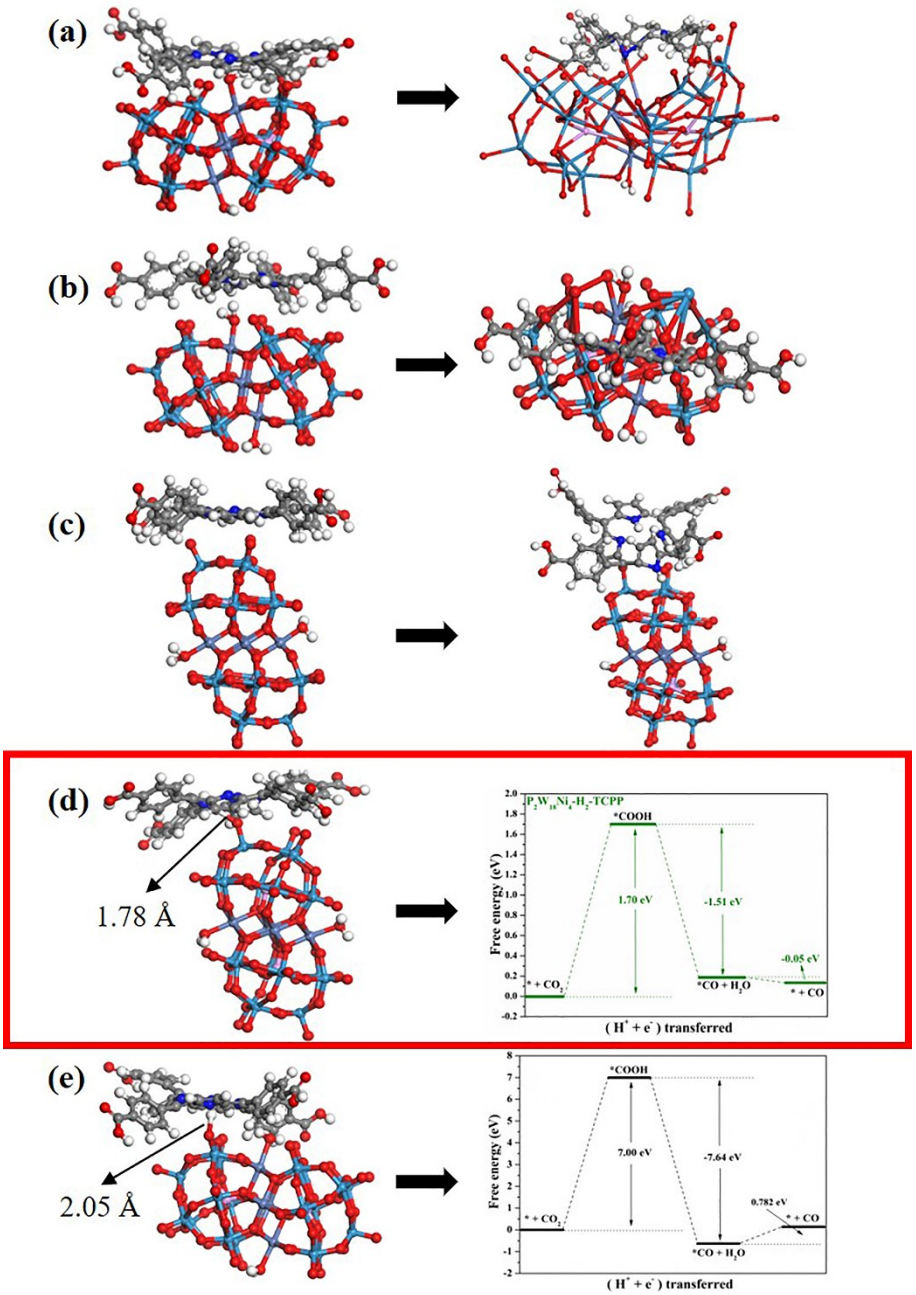

Figure S23. Five kinds of possible interactions between $P_2W_{18}M_4$ and H_2–TCPP; (a) M–OH_2–N (strong interaction); (b) M–OH_2···N (weak interaction); (c) W=O···N–H (weak interaction, W=O comes from the polar $\{W_3O_{10}\}$ cluster); (d) W=O–N–H (strong interaction, W=O comes from the polar $\{W_3O_{10}\}$ cluster); (e) W=O–N–H (strong interaction, W=O comes from the equatorial $\{W_3O_{10}\}$ cluster).

Reference

1 J. Y. Han, D. P. Wang, Y. H. Du, S. B. Xi, Z. Chen, S. M. Yin, T. H. Zhou and R. Xu, *Appl. Catal. A: Gen.*, 2016, **521**, 83–89.

2 S. Karamzadeh, E. Sanchooli, A. R. Oveisi, S. Daliran and R. Luque, *Appl. Catal. B*., 2022, **303**, 120815.

3 H. Wu, S. H. Fan, W. Y. Zhu, Z. Dai, X. Y. Zou, *Bisens. Bioelectron*., 2013, 589–594.

4 M. M. Conradie, J. Conradie, *Electrochim. Acta*, 2015, 512–519.

5 M. J. Liu, M. T. Peng, B. X. Dong, Y. L. Teng, L. G. Feng and Q. Xu, *Chin. J. Struct. Chem.*, 2022, **41**, 2207046–2207052.

6 M. García, M. J. Aguirre, G. Canzi, C. P. Kubiak, M. Ohlbaum and M. Isaacs, *Electrochim. Acta*., 2014, **115**, 146–154.

7 S. X. Guo, D. R. MacFarlane and J. Zhang, *ChemSusChem*., 2016, **9**, 80–87.

8 S. X. Guo, F. W. Li, L. Chen, D. R. MacFarlane and J. Zhang, *ACS Appl. Mater. Interfaces*., 2018, **10**, 12690−12697.

9 Y. R. Wang, Q. Huang, C. T. He, Y. F. Chen, J. Liu, F. C. Shen and Y. Q. Lan, *Nat. Commun.*, 2018, **9**, 4466.

10 M. Girardi, D. Platzer, S. Griveau, F. Bedioui, S. Alves, A. Proust and S. Blanchard, *Eur. J. Inorg. Chem*., 2019, 387–393.

11 J. Du, Z. L. Lang, Y. Y. Ma, H. Q. Tan, B. L. Liu, Y. H. Wang, Z. H. Kang and Y. G. Li, *Chem. Sci.*, 2020, **11**, 3007–3015.

12 D. J. Zang, Q. Li, G. Y. Dai, M. Y. Zeng, Y. C. Huang and Y. G. Wei, *Appl. Catal. B.*, 2021, **281**, 119426.

13 H. Z. Yang, D. R. Yang, Y. Zhou and X. Wang, *J. Am. Chem. Soc*., 2021, **143**, 13721−13730.

14 M. L. Sun, Y. R. Wang, W. W. He, R. L. Zhong, Q. Z. Liu, S. Y. Xu, J. M. Xu, X. L. Han, X. Y. Ge, S. L. Li, Y. Q. Lan, A. M. Al–Enizi, A. Nafady and S. Q. Ma, *Small.*, 2021, **17**, 2100762.

15 Z. F. Xin, Y. R. Wang, Y. F. Chen, W. L. Li, L. Z. Dong and Y. Q. Lan, *Nano Energy.*, 2020, **67**, 104233–104241.

16 Q. Wu, R. K. Xie, M. J. Mao, G. L. Chai, J. D. Yi, S. S. Zhao, Y. B. Huang and R. Cao, *ACS Energy Lett*., 2020, **5**, 1005−1012.

17 X. D. Zhang, S. Z. Hou, J. X. Wu and Z. Y. Gu, *Chem. Eur. J*., 2020, **26**, 1604−1611.

18 E. X. Chen, J. Yang, M. Qiu, X. Y. Wang, Y. F. Zhang, Y. J. Guo, S. L. Huang, Y. Y. Sun, J. Zhang, Y. Hou and Q. P. Lin, *ACS Appl. Mater. Interfaces*., 2020, **12**, 52588−52594.

19 C. B. Lu, J. Yang, S. C. Wei, S. Bi, Y. Xia, M. X. Chen, Y. Hou, M. Qiu, C. Yuan, Y. Z. Su, F. Zhang, H. W. Liang and X. D. Zhuang, *Adv. Funct. Mater*., 2019, **29**, 1806884−1806891.

20 Z. F. Xin, J. J. Liu, X. J. Wang, K. J. Shen, Z. B. Yuan, Y. F. Chen and Y. Q. Lan, *ACS Appl. Mater. Interfaces*., 2021, **13**, 54959−54966.

21 C. Wang, C. Y. Zhu, M. Zhang, Y. Geng, Y. G. Li and Z. M. Su, *J. Mater. Chem. A*., 2020, **8**, 14807–14814.